Optimizing Interface Conductivity in Electronics

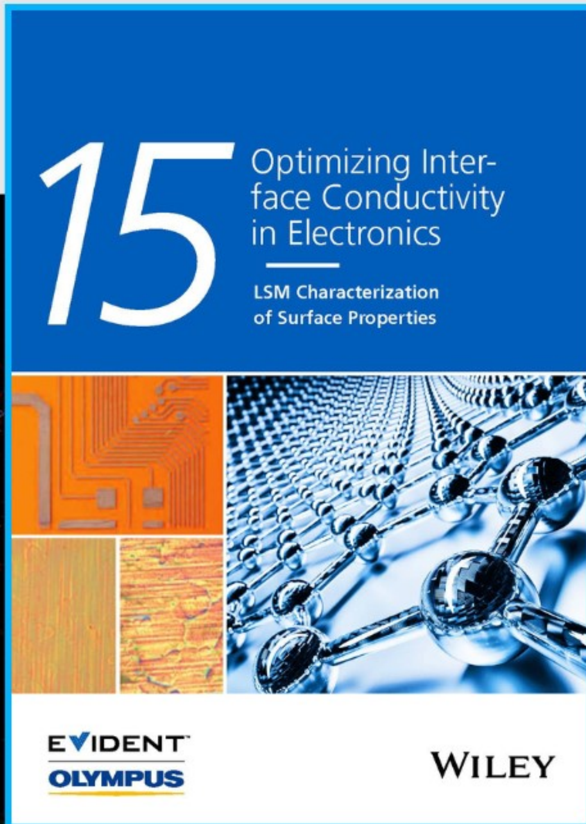

The latest eBook from Advanced Optical Metrology. Download for free.

Surface roughness is a key parameter for judging the performance of a given material's surface quality for its electronic application. A powerful tool to measure surface roughness is 3D laser scanning confocal microscopy (LSM), which will allow you to assess roughness and compare production and finishing methods, and improve these methods based on mathematical models.

Focus on creating high-conductivity electronic devices with minimal power loss using laser scanning microscopy is an effective tool to discern a variety of roughness parameters.

EVIDENT
OLYMPUS

WILEY

RESEARCH ARTICLE

ADVANCED ELECTRONIC MATERIALS Open Access

www.advelectronicmat.de

Check for updates

An Anti-Ambipolar Cryo-Phototransistor

Roshan Jesus Mathew, Kai-Hsiang Cheng, Christy Roshini Paul Inbaraj, Raman Sankar, Xuan P.A. Gao, and Yit-Tsong Chen**

Novel anti-ambipolar transistors (AATs) are gate tunable rectifiers with a marked potential for multi-valued logic circuits. In this work, the optoelectronic applications of AATs in cryogenic conditions are studied, of which the AAT devices consist of vertically stacked *p*-SnS and *n*- $MoSe_2$ nanoflakes to form a type-II staggered band alignment. An electrostatically tunable p-SnS/n-$MoSe_2$ cryo-phototransistor is presented with unique anti-ambipolar characteristics and cryogenic-enhanced optoelectronic performance. The cryo-phototransistor exhibits a sharp and highly symmetric anti-ambipolar transfer curve at 77 K with the peak-to-valley ratio of 10^3 operating under a low bias voltage of 1 V. The high cooling-enhanced charge mobilities in the cryo-phototransistor grant this AAT device remarkable photodetection capabilities. At 77 K, the *p*-SnS/*n*-$MoSe_2$ cryo-phototransistor, holding a broad photoresponse in the spectral range of 250–900 nm, demonstrates its high responsivity of 2×10^4 A W^{-1} and detectivity of 7.5×10^{13} Jones with the excitation at 532 nm. The high-performance *p*-SnS/*n*-$MoSe_2$ low-dimensional phototransistor with low operating voltages at 77–150 K is eligible for optoelectronic applications in cryogenic environments. Furthermore, the cryo-characteristics of this heterostructure can be further extended to design the mul-tivalued logic circuits operated in cryogenic conditions.

1. Introduction

2D layered materials with strong in-plane covalent bonds and weak out-of-plane van der Waals interactions exhibit extraordinary and unique physical properties. Among them, a wide variety of transition-metal dichalcogenides (TMDs)[1–3] and III–VI semiconductors of the *n*-type semiconducting nature[4,5] were investigated for their exotic device physics. In the midst of challenges to achieve high-performance *p*-type semiconductors, the anisotropic layered IV–VI metal monochalcogenide of tin sulfide (SnS) with a low-symmetry orthorhombic crystal structure[6] has presented its potential in solar cell[7] and thermoelectric applications.[8] However, the electrical-transport study on the nanoscale SnS crystal is still very limited due to the difficulty in obtaining thin SnS nanoflakes by mechanical exfoliation. The recent transport studies revealed good gate tunability in negative voltages of the exfoliated SnS multilayers, yet the carrier screening and rich intrinsic *p*-type doping warrant a significant output current from p-type carriers and restrain the device from a complete turn-off even at 250 K under high positive gate voltages.[9] The intrinsically *p*-doped nature of SnS makes it a good candidate in van der Waal heterostructure devices where a *p*-type layer is required.

To date, the partially stacked vertical *p-n* heterointerface transistors have been reported to show unique gate-tunable rectifying characteristics, analogous to negative differential resistance (NDR) but with a much higher peak-to-valley ratio, called as anti-ambipolar transistors (AATs).[10] The AATs holding the maximum conductance at a certain gate voltage (i.e., with an inverted V-shaped gate transfer curve), in contrast

R. J. Mathew, K.-H. Cheng, Y.-T. Chen
Department of Chemistry
National Taiwan University
Taipei 10617, Taiwan
E-mail: ytcchem@ntu.edu.tw; ytc22@nycu.edu.tw

R. J. Mathew, K.-H. Cheng, Y.-T. Chen
Institute of Atomic and Molecular Sciences
Academia Sinica
Taipei 10617, Taiwan

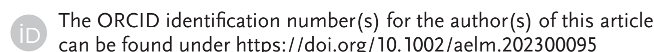
The ORCID identification number(s) for the author(s) of this article can be found under https://doi.org/10.1002/aelm.202300095

© 2023 The Authors. Advanced Electronic Materials published by Wiley-VCH GmbH. This is an open access article under the terms of the Creative Commons Attribution License, which permits use, distribution and reproduction in any medium, provided the original work is properly cited.

DOI: 10.1002/aelm.202300095

C. R. P. Inbaraj
Department of Physics
National Taiwan University
Taipei 10617, Taiwan

R. Sankar
Institute of Physics
Academia Sinica
Taipei 11529, Taiwan

X. P. Gao
Department of Physics
Case Western Reserve University
Cleveland, Ohio 44106, USA
E-mail: xuan.gao@case.edu

Y.-T. Chen
Department of Electrophysics, PSMC-NYCU Research Center, and LIGHTMED Laser System Research Center
National Yang Ming Chiao Tung University
Hsinchu 300093, Taiwan

2199160x, 2023, 8, Downloaded from https://onlinelibrary.wiley.com/doi/10.1002/aelm.202300095 by National Yang Ming Chao Tung Unive, Wiley Online Library on [14/08/2023]. See the Terms and Conditions (https://onlinelibrary.wiley.com/terms-and-conditions) on Wiley Online Library for rules of use; OA articles are governed by the applicable Creative Commons License

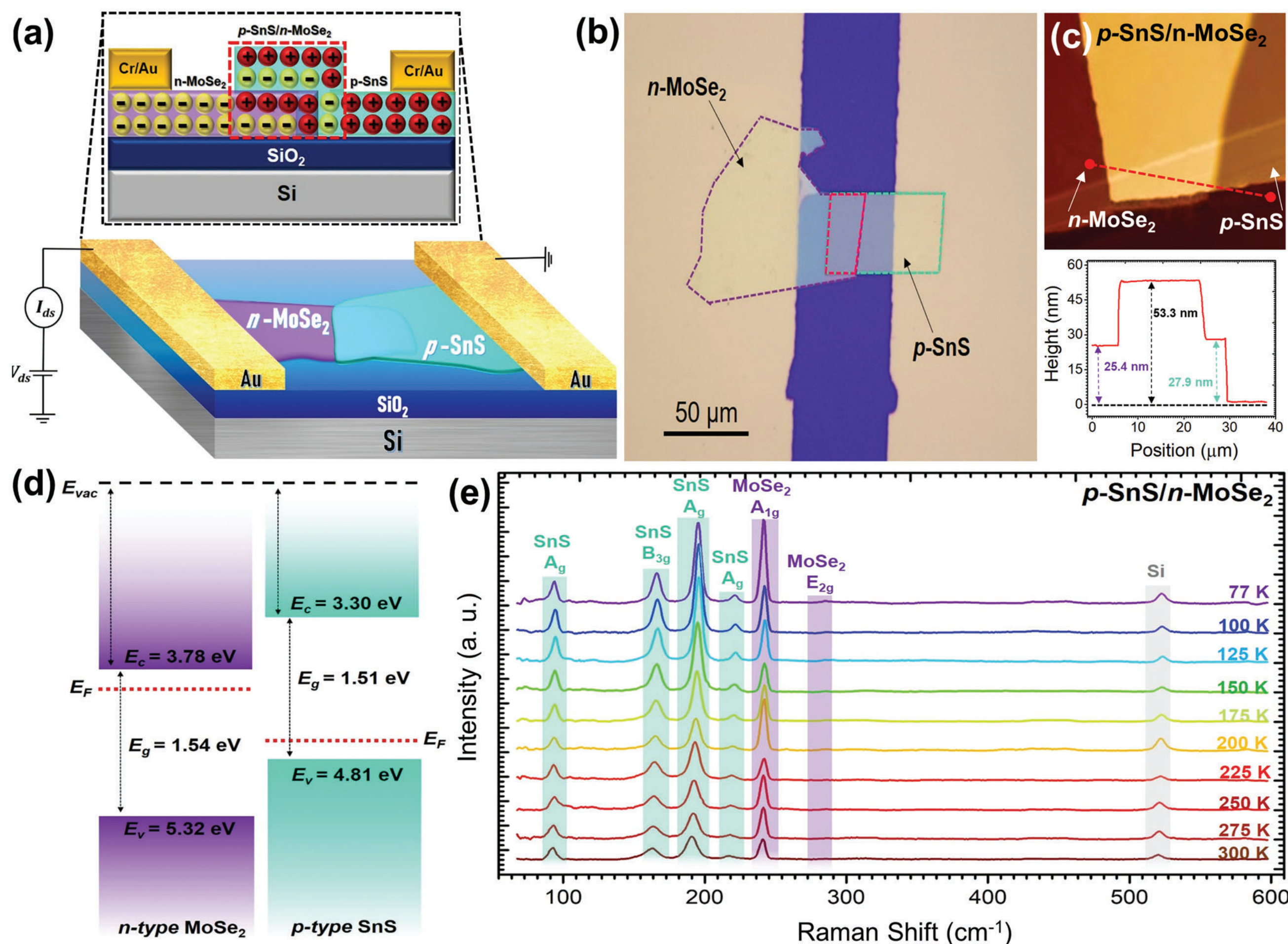

Figure 1. a) An AAT device comprising the p-SnS/n-$MoSe_2$ heterostructure is illustrated with the cross-sectional view of this p-n junction depicted in the inset. b) An optical microscopic image of the as-fabricated AAT device shows the p-SnS/n-$MoSe_2$ heterostructure with c) the corresponding topographical image and a height profile along the red dashed line. d) An energy diagram represents the band alignment for p-SnS and n-$MoSe_2$. e) Temperature-dependent Raman scattering spectra of the p-SnS/n-$MoSe_2$ heterostructure were observed at 77–300 K.

to ordinary ambipolar transistors (with a V-shaped gate transfer curve),[11] have been demonstrated advantageous for implementing simplified circuits.[10] Since it utilizes a single p-n junction to generate both positive and negative transconductances with an enabling switch between these two states in a device, AATs become a promising constituent in the place of multi-valued logic (MVL) devices.[10,12–14]

Although a few AATs composed of organic materials, organic/TMD,[15,16] TMD/TMD,[14,17] and a very recent bi-anti-ambipolar flexible transistor have been investigated,[12] there is no report so far on the temperature effects on the electrical transports and photodetections of anti-ambipolar heterotransistors. Low-dimensional cryogenic transistors exhibit the advantages of not only the enhanced mobility, circuit integration density, and power density, but also the reductions of power consumption, interconnection resistance, and thermally activated degradations.[18] As for photoresponsivity, one of the critical figures of merit of a photodetector counts the mobility and density of the photogenerated carriers,[19] where the intrinsic optoelectronic properties of the heterojunction channel can be improved at ultra-low temperatures. Among optoelectronic devices, the photodetectors covering the spectral range from ultraviolet to infrared have wide application in optical communication, chemical analysis, image sensing, and astronomy.[20,21] Moreover, a broadband photodetector capable of working in the low operating temperature window is highly demanded for space exploration, research in the polar regions, and cryostat instrumentations.[22] In this context, we present an electrostatically tunable cryo-heterotransistor device, by integrating p-type SnS nanoflakes of high carrier density and n-type $MoSe_2$ (molybdenum diselenide) nanoflakes of strong positive gating feature to form a type-II staggered band alignment, which demonstrates unique anti-ambipolar characteristics and cryogenic-enhanced optoelectrical performance.

2. Results and Discussion

As illustrated in **Figure 1**a, AATs were fabricated with a van der Waals assembly of heterojunction between the few-layered nanoflakes of p-SnS and n-$MoSe_2$, which were electrically contacted by Cr/Au (7 nm/70 nm in thickness) electrodes with a p-doped Si back-gate. In the as-fabricated AATs, n-$MoSe_2$ was cho-

 © 2023 The Authors. Advanced Electronic Materials published by Wiley-VCH GmbH

2199160x, 2023, 8, Downloaded from https://onlinelibrary.wiley.com/doi/10.1002/aelm.202300095 by National Yang Ming Chiao Tung Unive, Wiley Online Library on [14/08/2023]. See the Terms and Conditions (https://onlinelibrary.wiley.com/terms-and-conditions) on Wiley Online Library for rules of use; OA articles are governed by the applicable Creative Commons License

sen because of its strong positive gating characteristics in cryogenic conditions;[23] in addition, the band alignment of *n*-$MoSe_2$ with *p*-SnS constructs a type-II staggered band diagram. Owing to the difficulty in obtaining uniform thin *p*-SnS nanoflakes from mechanical exfoliation, the *p*-SnS samples were grown with a chemical vapor deposition (CVD) method, whereas the *n*-$MoSe_2$ layers were exfoliated from its bulk single crystals grown in chemical vapor transport (CVT) method (the synthesis methods are described in Sections S1 and S2 and Figures S1 and S2, Supporting Information). The as-synthesized samples exhibit high crystallinity and perfect composition ratio as characterized by microscopy and spectroscopy (Figure S3 in Section S3 and Figure S4 in Section S4, Supporting Information). In this AAT work, few-layered *p*-SnS and *n*-$MoSe_2$ nanoflakes were selected as we noted that sufficient carrier concentrations in nano-layers play a key role in the AAT performance.[14] A dry transfer method using polydimethylsiloxane (PDMS) stamps was employed for a clean, contamination-free assembly of the high-quality stoichiometric *p*-SnS/*n*-$MoSe_2$ heterostructure. The assembling process for the *p*-SnS/*n*-$MoSe_2$ heterostructure is detailed in the Experimental Section. Hereafter, the *p*-SnS/*n*-$MoSe_2$ notation represents that *p*-SnS is on top of *n*-$MoSe_2$ laid on a SiO_2/Si supporting substrate (i.e., a Si wafer). The *p*-SnS and *n*-$MoSe_2$ nanoflakes of ≈27.9 and ≈25.4 nm in thicknesses, respectively (Figure 1b,c), were aligned to form a type-II heterostructure (Figure 1d). The work functions of the *p*-SnS and *n*-$MoSe_2$ nanoflakes were examined by ultraviolet photoelectron spectroscopy (UPS, in Section S5 and Figure S5, Supporting Information), giving the bandgaps of 1.51 and 1.54 eV, respectively, to assist the band alignment in the energy diagram.

The temperature-dependent Raman scattering spectroscopy of the *p*-SnS/*n*-$MoSe_2$ heterojunction and individual *p*-SnS and *n*-$MoSe_2$ nanoflakes were observed and analyzed in Figure 1e and Figure S6 in Section S6 (Supporting Information). At room temperature, the prominent Raman signal of *n*-$MoSe_2$ at 242 cm^{-1} results from the out-of-plane vibration of the A_{1g} phonon mode, which involves the opposing vibrations of the two Se atoms with respect to the Mo atom.[24,25] On the other hand, *p*-SnS possesses three distinctive vibrational signals at 161, 189, and 217 cm^{-1}.[26] While the B_{3g} and A_g phonon modes of the "NaCl" type vibration are responsible for the 161 and 217 cm^{-1} peaks, respectively, the 189 cm^{-1} signal originates from the A_g "breathing" phonon mode of *p*-SnS (Figure S6, Supporting Information).[27] The temperature-dependent Raman analysis in Figure 1e reveals that all the prominent peaks of *p*-SnS and *n*-$MoSe_2$ appear in the overlapped *p*-SnS/*n*-$MoSe_2$ junction region. The temperature-induced variation in the full width at half maximum (FWHM) of the observed peaks is attributed to the double-resonance phenomenon due to phonon dispersion.[28] Notably, no additional peaks exist in the junction region, clearly pointing out the absence of interlayer vibrations in the *p*-SnS/*n*-$MoSe_2$ heterointerface.

Figure 2 shows the temperature-dependent photoluminescence (PL) of *p*-SnS/*n*-$MoSe_2$, which reveals the optical illuminating properties of this heterostructure. In Figure 2a, three PL signals of *p*-SnS centered at 1.27, 1.56, and 1.67 eV were observed at 77 K and exhibited slight red shifts with increasing temperature. According to the valley-selectivity analysis in the linearly polarized emission at non-degenerate bandgaps,[29] the PL signals at 1.27 and 1.56 eV occur, respectively, at the ΓX and ΓY valleys of *p*-SnS, whereas the PL of 1.67 eV could take place at the ΓY valley or might be due to higher order transitions. In Figure 2b, the PL peaks of *n*-$MoSe_2$ at 1.61 and 1.85 eV measured at 77 K were reported resulting from the A and B excitons, respectively.[30] These PL signals also display red shifts with increasing temperature. The red shifts stem from the lattice expansion in the *n*-$MoSe_2$ crystal as temperature raises, consequently reducing the potential confinement and decreasing the energy bandgap. Meanwhile, the PL intensities are noted to increase with decreasing temperature, implying the lifetimes of both A and B excitons in *n*-$MoSe_2$ were augmented at low temperatures due to the reduced thermal vibrations to suppress nonradiative electron-hole recombinations.[31]

Figure 2c,d presents the temperature-dependent PL intensities of the *p*-SnS/*n*-$MoSe_2$ heterostructure. It is important to note that the PL spectra of the *p*-SnS/*n*-$MoSe_2$ heterojunction (Figure 2c) include all of the constituent signals from individual *p*-SnS and *n*-$MoSe_2$, without other additional peaks, manifesting no interlayer excitonic recombination in the junction region. In Figure 2c,d, the relatively stronger (weaker) PL intensity of the *p*-SnS (*n*-$MoSe_2$) at 77 K is due to the stacking order of the upper *p*-SnS (lower *n*-$MoSe_2$) on the heterojunction. However, their relative PL intensities reverse as temperature increases. This phenomenon also demonstrates that as temperature increases beyond 150 K, *p*-SnS weakens, but *n*-$MoSe_2$ dominates, the illuminating properties of the heterointerface, suggesting the *p*-SnS/*n*-$MoSe_2$ heterostructure to hold potential applications in a cryogenic environment.

Figure 3a,b shows the temperature-dependent electrical-transport measurements of the *n*-$MoSe_2$-based and *p*-SnS-based transistors fabricated on a SiO_2/Si substrate by sweeping the back-gate voltage (V_g) with a constant bias voltage (V_{sd}) of 1 V. As temperature increases, the drastic shifts of the threshold voltage (V_{th}) were observed in both *n*-$MoSe_2$ and *p*-SnS transistors (summarized in Figure S7 of Section S7, Supporting Information). From 77 to 300 K, the "ON states" of the *n*-$MoSe_2$ transistor were achieved at $V_g > V_{th}$ with V_{th} varying from −0.9 to −43 V, whereas the *p*-SnS device was turned on at $V_g < V_{th}$ with V_{th} changing from 1 to 75 V under the similar conditions. The measured transfer characteristics confirm the *n*-$MoSe_2$ and *p*-SnS transistors, respectively, holding electrons and holes as the majority charge carriers. With increasing temperature, the *n*-$MoSe_2$ transistor shows a gradual increase of the source-drain current (I_{sd}) at $V_g = -40$ to 20 V, but then a slight decrease of I_{sd} within $V_g = 20-60$ V. Similar transport characteristics were observed in the output current (I_{sd}) of the *p*-SnS transistor, i.e., increasing at $V_g = 100$ to −15 V but then decreasing at $V_g = -15$ to −30 V. In the cryogenic conditions at 77 K, the on/off ratios of 2.3×10^5 (*p*-SnS) and 3×10^2 (*n*-$MoSe_2$) at $V_{sd} = 1$ V were measured and the effective field-effect carrier mobilities, $\mu = L/(WCV_{sd})\cdot(dI_{sd}/dV_g)$, of ≈1.37 $cm^2\ V^{-1}\ s^{-1}$ for *p*-SnS and ≈6.9 $cm^2\ V^{-1}\ s^{-1}$ for *n*-$MoSe_2$ were extracted from the transfer curves in the linear regime. The determined μ values are comparable to those of the recently reported *p*-SnS-based and *n*-$MoSe_2$-based field-effect transistors. As temperature increases, both *p*-SnS and *n*-$MoSe_2$ transistors exhibit a decrease in the mobility and sharp drop in the on/off ratio as shown in

© 2023 The Authors. Advanced Electronic Materials published by Wiley-VCH GmbH

2199160x, 2023, 8, Downloaded from https://onlinelibrary.wiley.com/doi/10.1002/aelm.202300095 by National Yang Ming Chiao Tung Unive, Wiley Online Library on [14/08/2023]. See the Terms and Conditions (https://onlinelibrary.wiley.com/terms-and-conditions) on Wiley Online Library for rules of use; OA articles are governed by the applicable Creative Commons License

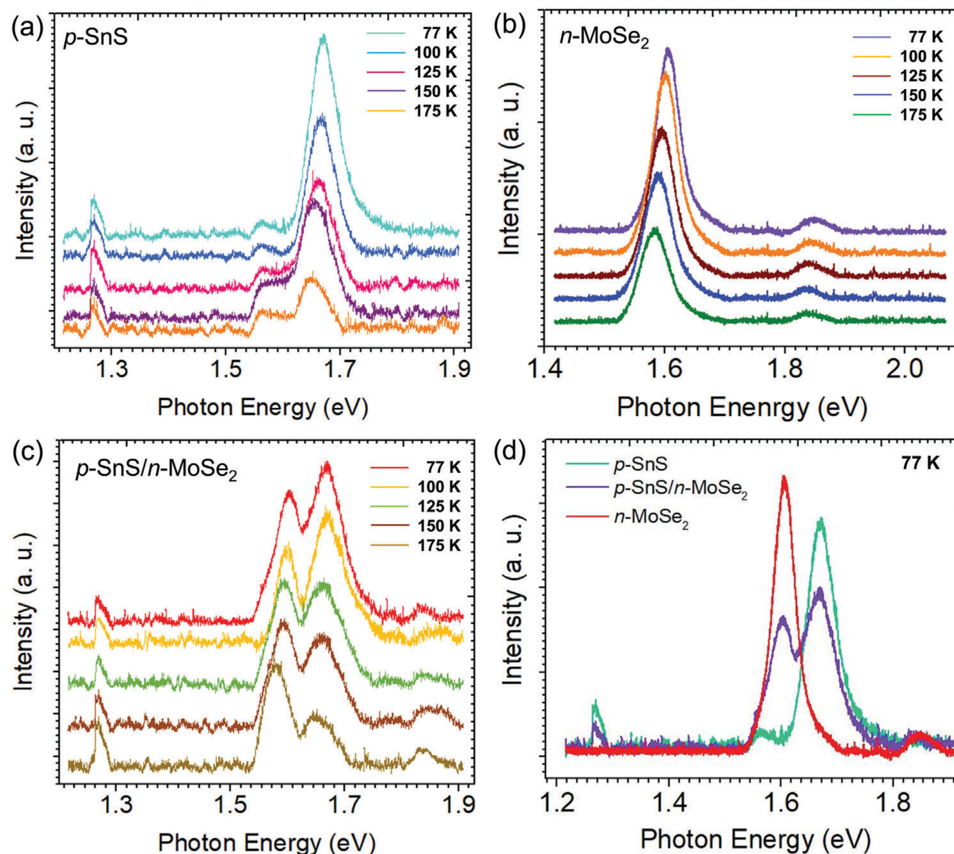

Figure 2. Temperature-dependent PL spectra of a) p-SnS nanoflakes, b) n-$MoSe_2$ nanoflakes, and c) the p-SnS/n-$MoSe_2$ heterojunction in the temperature range from 77 to 175 K. d) The PL spectra of p-SnS, n-$MoSe_2$, and p-SnS/n-$MoSe_2$ at 77 K. All of the PL spectra were taken with 532 nm laser excitation.

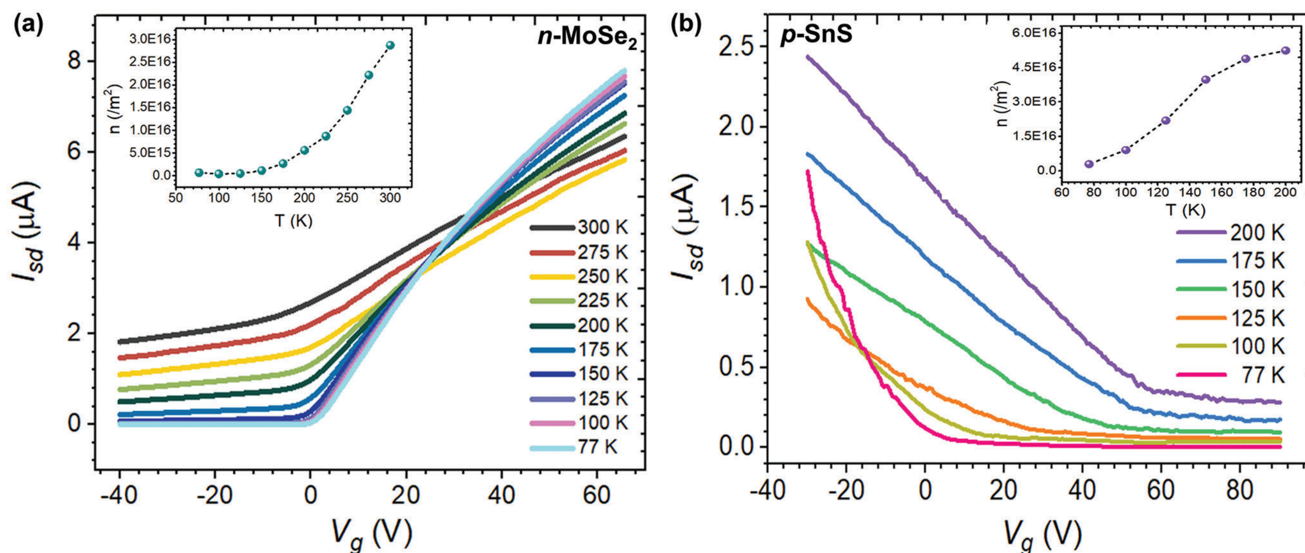

Figure 3. Temperature-dependent electrical properties of a) n-$MoSe_2$ and b) p-SnS transistors were measured at V_{sd} = 1 V and various V_g values. The insets show the corresponding temperature-dependent carrier concentrations in the transistors.

© 2023 The Authors. Advanced Electronic Materials published by Wiley-VCH GmbH

2199160x, 2023, 8, Downloaded from https://onlinelibrary.wiley.com/doi/10.1002/aelm.202300095 by National Yang Ming Chao Tung Unive, Wiley Online Library on [14/08/2023]. See the Terms and Conditions (https://onlinelibrary.wiley.com/terms-and-conditions) on Wiley Online Library for rules of use; OA articles are governed by the applicable Creative Commons License

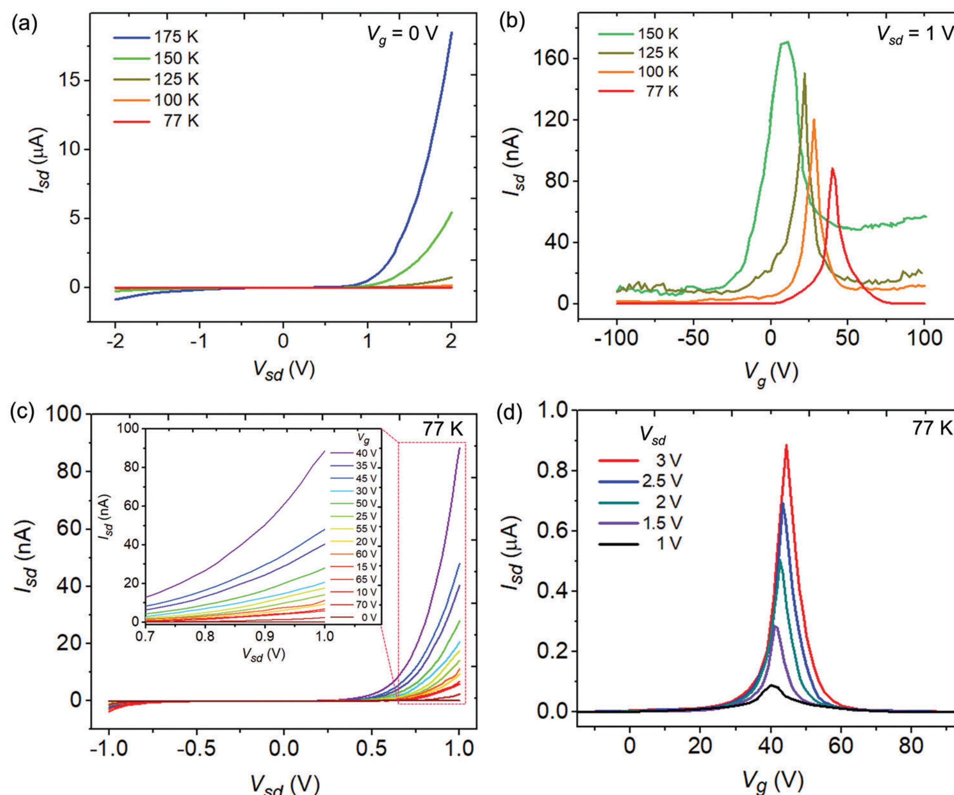

Figure 4. a,b) Temperature-dependent transport characteristics of the *p*-SnS/*n*-$MoSe_2$ heterotransistor were measured in response to the applied bias voltages and gate voltages. c,d) The gate-dependent output curves and bias voltage-dependent transfer curves of the *p*-SnS/*n*-$MoSe_2$ heterotransistor were measured at 77 K.

Figures S8–S10 of Section S8 (Supporting Information), showing the significant impact of thermally excited carriers on the device performance in this temperature range.

From the measured V_{th} value at each temperature, the carrier concentration (n) of the individual *n*-$MoSe_2$ and *p*-SnS channels at $V_g = 0$ V were estimated by $n = q^{-1}\ C_g\ |V_{th}|$ with the elementary charge of $q = 1.6 \times 10^{-19}$ C and the capacitance of $C_g = 1.23 \times 10^{-8}$ F cm^{-2} for 300 nm-thick SiO_2 dielectric layer.[32] In the insets of Figure 3a,b, both *n*-$MoSe_2$ and *p*-SnS nanoflakes show an increase of the carrier concentration with increasing temperature from 77 K, reflecting the thermally excited carriers from unintentionally doped impurities. Both *n*-$MoSe_2$ and *p*-SnS nanoflakes display strong gate tunability even at low operational temperatures (77–150 K), manifesting the potential to form tunable *p-n* junctions at cryogenic conditions. However, it is noted although the overall range of the carrier concentrations in *p*-SnS and *n*-$MoSe_2$ is $\approx 10^{16}$/m^2, these two materials do have quite different carrier concentrations at the same temperature and their characteristic carrier activation temperatures are different. For example, at 200 K, the carrier concentration is $\approx 5 \times 10^{16}$/m^2 in *p*-SnS but is only $\approx 5 \times 10^{15}$/ m^2 in *n*-$MoSe_2$ with the difference in the carrier concentrations by about a factor of ten. Moreover, in *n*-$MoSe_2$, the carrier density drops quickly toward zero as temperature decreases, but in *p*-SnS, the carriers do not freeze out so rapidly, suggesting a smaller activation energy for the dopants in *p*-SnS, presumably due to the acceptor levels being close to the valence band of SnS. Consequently, as the temperature increases, the symmetric anti-ambipolarity of the *p*-SnS/*n*-$MoSe_2$ heterojunction disappears because of the unbalanced carrier concentrations in the *p*- and *n*-channels.

Figure 4a shows the temperature-dependent output characteristics of the *p*-SnS/*n*-$MoSe_2$ heterojunction (as illustrated in Figure 1a) at $V_g = 0$ V and $V_{sd} = -2$–2 V, displaying excellent *p-n* junction behavior in the temperature range from 77 to 175 K. The heterojunction transistor turns on at $V_{sd} < 1$ V for all temperatures measured, revealing the low-voltage operation of the heterojunction device irrespective of temperature. Moreover, the transfer curves (measured at $V_{sd} = 1$ V and $V_g = -100$–100 V, Figure 4b) demonstrate anti-ambipolar behavior with a prominent peak voltage that shifts from ≈40 V to ≈0 V under cryogenic conditions at 77−150 K. This is because the anti-ambipolar transistor's ON state happens when both the *n*- and *p*-channels are conductive,[10] but the carriers freeze out in $MoSe_2$ and SnS with different temperature dependences (or the threshold voltages for $MoSe_2$ and SnS shift with temperature at different rates) (Figure 3). With increasing temperature from 77 to 150 K, the I_{sd} of the anti-ambipolar peak roughly enhances by a factor of two, and the corresponding peak V_g for the maximal I_{sd} reduces from ≈40 V toward zero, which is more favorable for the device operation from the gate-voltage requirement perspective. However, a more symmetric anti-ambipolar shape was observed at 77 K where both electrons and holes possess almost the same

© 2023 The Authors. Advanced Electronic Materials published by Wiley-VCH GmbH

2199160x, 2023, 8, Downloaded from https://onlinelibrary.wiley.com/doi/10.1002/aelm.202300095 by National Yang Ming Chiao Tung Unive, Wiley Online Library on [14/08/2023]. See the Terms and Conditions (https://onlinelibrary.wiley.com/terms-and-conditions) on Wiley Online Library for rules of use; OA articles are governed by the applicable Creative Commons License

mobilities of 1.54 and 1.56 $cm^2\ V^{-1}\ s^{-1}$, respectively, and the anti-ambipolar transistor's on/off, or peak/valley, ratio is much higher, reaching 4.28×10^3 and 5.0×10^3 on the electron and hole side (Section S8 and Figure S10, Supporting Information). When temperature increases to 150 K, the symmetric shape is distorted, leading to the saturation in the *p*-type region. This phenomenon is due to the heavily doped nature of *p*-SnS, which resists the device to be turned off completely at escalated temperature.[9]

In Figure 4c, we further studied the symmetric anti-ambipolar behavior at 77 K by measuring the gate-dependent output characteristics of the *p*-SnS/*n*-$MoSe_2$ heterotransistor at $V_g = 0–70$ V with a stepwise increase of 5 V. It is interesting to note in the inset of Figure 4c that the I_{sd} measured at $V_g = 40$ V not only reaches the maximum, but also rises far above those measured at other V_g values, consistent with the symmetric anti-ambipolar nature of the *p*-SnS/*n*-$MoSe_2$ heterojunction transistor (i.e., the symmetric curve at 77 K in Figure 4b peaked at $V_g = 40$ V). But, this phenomenon disappears at room temperature as the high carrier concentration of *p*-SnS at room temperature constrains the anti-ambipolar nature. This outcome also justifies the aforementioned carrier-concentration analyses of *n*-$MoSe_2$ and *p*-SnS displayed in the insets of Figure 3a,b. The carrier concentration in *p*-SnS is more enhanced than in *n*-$MoSe_2$ with elevated temperature, resulting in breaking the symmetric anti-ambipolarity in the *p*-SnS/*n*-$MoSe_2$ heterojunction at the temperature above 125 K. Moreover, the *p*-SnS/*n*-$MoSe_2$ heterotransistor lost its anti-ambipolarity completely at room temperature and exhibited rectifying behavior at both positive and negative V_{sd} without its diode characteristic observed at low temperatures (Section S9 and Figure S11, Supporting Information). Furthermore, as shown in Figure 4d, when both hole-dominant *p*-SnS and electron-dominant *n*-$MoSe_2$ are in their "ON states" at 0 V $< V_g <$ 70 V, the *p*-SnS/*n*-$MoSe_2$ heterotransistor holds the symmetric anti-ambipolar characteristics with various bias voltages.

In **Figure 5**, we elucidate the carrier transport in the *p*-SnS/*n*-$MoSe_2$ heterojunction by classifying the anti-ambipolar transfer curve into three divisions, *Zone A* ($V_g < 0$ V), *Zone B* (0 V $< V_g <$ 70 V), and *Zone C* (70 V $< V_g <$ 100 V), where the carrier transport mechanism in each zone can be interpreted with the corresponding schematic illustration (in the insets of Figure 5). Initially, the *p*-SnS/*n*-$MoSe_2$ heterojunction holds an equilibrium state in the non-biased condition. At *Zone A*, while sweeping V_g from −100 to 0 V at a constant $V_{sd} = 1$ V, *p*-SnS becomes conductive because of the accumulation of holes, whereas *n*-$MoSe_2$ is non-conductive as the flow of electrons is hindered by the negative V_g. Hence, the heterotransistor is in the "OFF state", generating very low I_{sd}. At *Zone B* (0 V $< V_g <$ 70 V), electrons and holes flow through *n*-$MoSe_2$ and *p*-SnS, respectively, making both devices conductive as they are operating beyond their V_{th} ranges. In the meantime, the *p*-SnS/*n*-$MoSe_2$ heterotransistor is in the "ON state" and exhibits the maximal conductance with a transient current spike. At *Zone C*, when *p*-SnS/*n*-$MoSe_2$ is subjected to 70 V $< V_g <$ 100 V, the conductive *n*-$MoSe_2$ and non-conductive *p*-SnS are resulted from the accumulated electrons and dissipated holes, respectively, leading to the "OFF state". In short, at *Zones A* and *C*, the transport of holes or electrons takes place only in one (either *p*- or *n*-) channel, thus restraining the conductivity of the heterotransistor. In contrast, when both channels are conductive at *Zone B* in a certain V_g range, the anti-ambipolar transfer characteristic with a peaked current is created. At 77 K and $V_{sd} = 1$ V, the maximal conductance of the *p*-SnS/*n*-$MoSe_2$ heterotransistor occurred at $V_g \approx 40$ V with the peak-to-valley ratio (i.e., $(I_{sd})_{max}/(I_{sd})_{min}$) of 10^3 and driving voltage ($\Delta V_g = (V_g)_{on} - (V_g)_{off}$) of ≈20 V. Notably, in view of these ambipolar characteristics of peak-to-valley ratio and driving voltage, this *p*-SnS/*n*-$MoSe_2$ heterotransistor, operated at low $V_{sd} \approx 1$ V, is superior to organic/TMD anti-ambipolar transistors[15,16] and comparable to TMD/TMD anti-ambipolar transistors.[14,17]

In **Figure 6**, the cooling-enhanced electrical property of the *p*-SnS/*n*-$MoSe_2$ heterojunction was further investigated by studying the photoresponsive performance of a *p*-SnS/*n*-$MoSe_2$ heterotransistor in the cryogenic environment at 77 K. The broadband spectral response, represented by photocurrent (I_{ph}) or photoresponsivity (R_λ), of a *p*-SnS/*n*-$MoSe_2$ phototransistor is observed in Figure 6a with the excitation light wavelength (λ) of 250–900 nm. The photoresponsivity ($R_\lambda = I_{ph}/PS$) of a phototransistor is defined as the ratio of the generated photocurrent ($I_{ph} = I_{light} - I_{dark}$) in response to the optical power density (P) impinging on the detector (S: illuminated area). The wavelength-dependent I_{ph} showed two spectral spikes at 2.61 eV (475 nm) and 2.36 eV (525 nm) in line with the absorption peaks of *n*-$MoSe_2$[34] and *p*-SnS,[35] respectively. The power-dependent output curves of the anti-ambipolar heterotransistor (Figure 6b) were also measured at $V_g = 40$ V with a 532-nm excitation laser of the power density from 40 μW cm^{-2} to 81.5 mW cm^{-2}. Moreover, the spectral response shows an increase of I_{ph} in the reverse bias conditions, revealing that the output current was produced largely by photo-induction, rather than field-generation, in support of the *p*-SnS/*n*-$MoSe_2$ device suitable for a good photodetector.

In Figure 6c, the obtained I_{ph} values (blue solid dots) exhibit a sublinear increase following a power law of I_{ph}–$P^{0.30}$ (blue line). The laser power-dependent R_λ can be attributed to the trap states in the interfaces of *p*-SnS/*n*-$MoSe_2$ and/or among *p*-SnS/*n*-$MoSe_2$/SiO_2/Si.[36] Interestingly, the measured R_λ values (red squares in Figure 6c) of the *p*-SnS/*n*-$MoSe_2$ phototransistor at $V_{sd} = -5$ V depend on the 532-nm illumination density by R_λ–$P^{-0.70}$ (red line), reaching very high $R_\lambda \approx 2 \times 10^4$ A W^{-1} with very low $P \approx 40$ μW cm^{-2}. This R_λ value acquired by our *p*-SnS/*n*-$MoSe_2$ phototransistor at cryogenic conditions is enhanced by orders of magnitude in comparison with those reported values of 2D heterostructured photodetectors operated at room temperature,[37] justifying the *p*-SnS/*n*-$MoSe_2$ phototransistor as a promising candidate for cryogenic applications.

The detectivity (D^*), defined as $D^* = R_\lambda S^{1/2}/(2eI_{dark})^{1/2}$, is used to quantify the ability of a photodetector for detecting weak optical signals (Section S10, Supporting Information). The high $D^* \approx 7.5 \times 10^{13}$ Jones measured at 77 K for the *p*-SnS/*n*-$MoSe_2$ phototransistor (illuminated with 40 μW cm^{-2} and operated at $V_g = 40$ V and $V_{sd} = -5$ V) is due to its low I_{dark} and high R_λ. The obtained D^* is similar with the recently reported room-temperature 2D material-based photodetectors[38–41] and is comparable to the commercial Si (10^{13} Jones) and InGaAs (10^{12-13} Jones)-based photodiodes.[42] The number of electrons detected per incident photon is defined by photogain, $\eta = R_\lambda hc/e\lambda$, for which the *p*-SnS/*n*-$MoSe_2$ phototransistor possesses $\eta = 6.7 \times 10^4$ at 77 K with the incident light of 40 μW cm^{-2} and electrical connections of $V_g = 40$ V, and $V_{sd} = -5$ V. The enhanced η of this phototransistor is due to the higher optical absorption of the

© 2023 The Authors. Advanced Electronic Materials published by Wiley-VCH GmbH

2199160x, 2023, 8, Downloaded from https://onlinelibrary.wiley.com/doi/10.1002/aelm.202300095 by National Yang Ming Chiao Tung Unive, Wiley Online Library on [14/08/2023]. See the Terms and Conditions (https://onlinelibrary.wiley.com/terms-and-conditions) on Wiley Online Library for rules of use; OA articles are governed by the applicable Creative Commons License

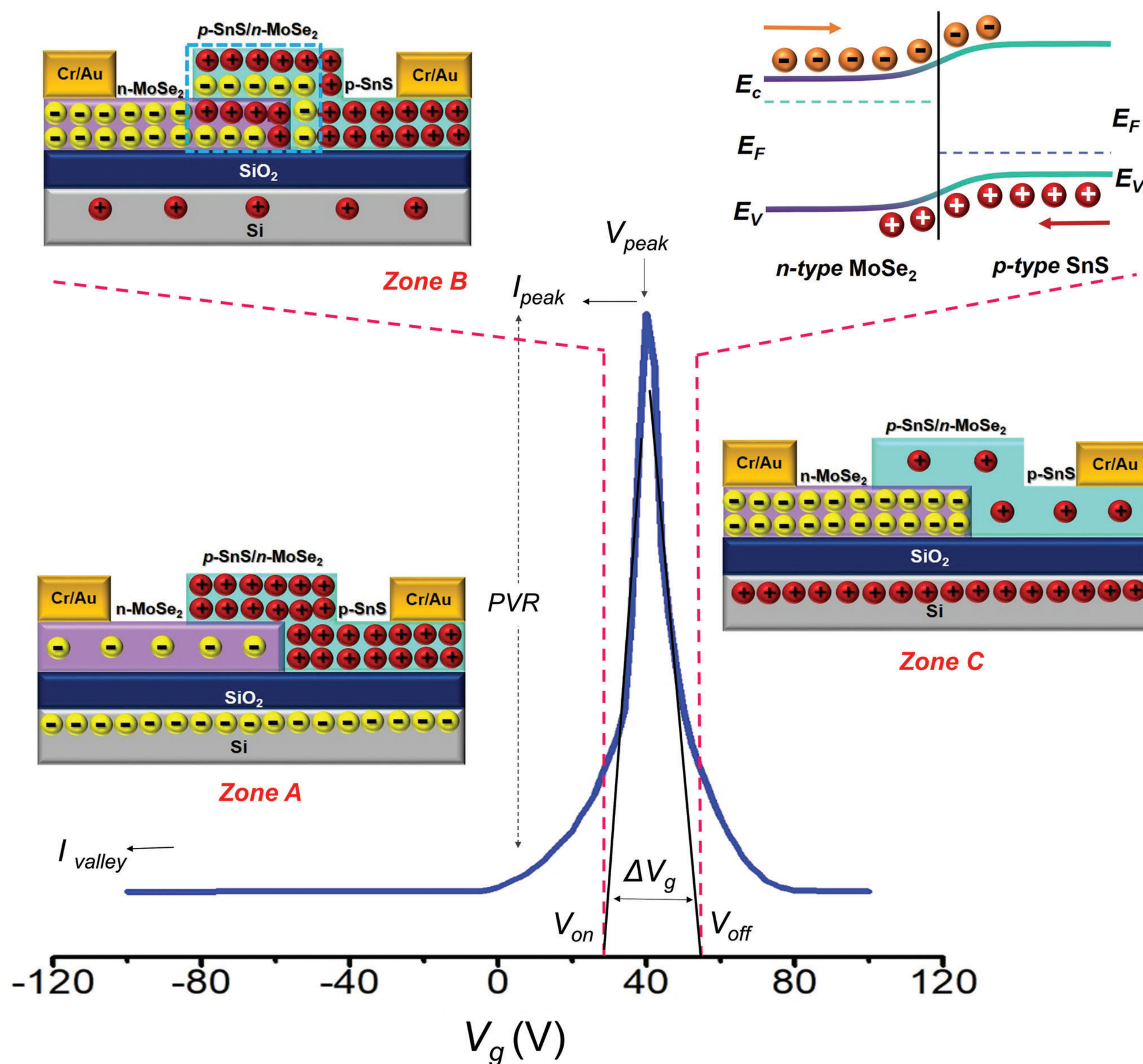

Figure 5. A charge-transport mechanism is proposed to schematically elucidate the electrical characteristics of the anti-ambipolar *p*-SnS/*n*-MoSe$_2$ heterotransistor operated at 77 K and low bias-voltage of $V_{sd} \approx 1$ V. (The transfer curve is extracted from that in Figure 4b). In the illustration, the device performance parameters are expressed by the peak-to-valley ratio (PVR = I_{peak}/I_{valley} with I_{peak} and I_{valley} being the maximal and minimal source-drain currents, respectively), the driving voltage (V_{peak}), and the on-state bias range ($\Delta V_g = V_{off} - V_{on}$ with V_{on} and V_{off} being the onset and offset gate voltages, respectively). The V_{on} and V_{off} values are the intercepted gate voltages determined by extrapolating the slopes of the transfer curve.[33]

p-SnS/*n*-MoSe$_2$ heterojunction with fewer interfacial trap states and reduced recombination rates.[41] Figure 6d presents the determined D^* and η of the *p*-SnS/*n*-MoSe$_2$ phototransistor as a function of incident laser power. At 77 K, the photoswitching of *p*-SnS/*n*-MoSe$_2$ in response to 532-nm laser illumination (with $P = 40$ µW cm^{-2}, $V_{sd} = -1$ V, and $V_g = 40$ V) is shown in Section S11 and Figure S12 (Supporting Information), where the device stability of the phototransistor was demonstrated by maintaining a constant current flow under a train of on-off switchings with the rising and falling times estimated 154 and 157 ms, respectively.

3. Conclusion

The *p*-SnS and *n*-MoSe$_2$ nanoflakes of high carrier densities were integrated to a *p-n* junction heterotransistor with the type-II band alignment. Electrical transports of the *p*-SnS/*n*-MoSe$_2$ heterotransistor were measured in the cryogenic conditions from 77 to 150 K, revealing the device's highly symmetric anti-ambipolar transfer characteristic at 77 K. The temperature-dependent Raman and PL studies provide the optical properties of the *p*-SnS/*n*-MoSe$_2$ heterostructure in extreme temperature conditions. At 77 K, the cooling-enhanced high mobility of the *p*-SnS/*n*-MoSe$_2$

© 2023 The Authors. Advanced Electronic Materials published by Wiley-VCH GmbH

2199160x, 2023, 8, Downloaded from https://onlinelibrary.wiley.com/doi/10.1002/aelm.202300095 by National Yang Ming Chao Tung Unive, Wiley Online Library on [14/08/2023]. See the Terms and Conditions (https://onlinelibrary.wiley.com/terms-and-conditions) on Wiley Online Library for rules of use; OA articles are governed by the applicable Creative Commons License

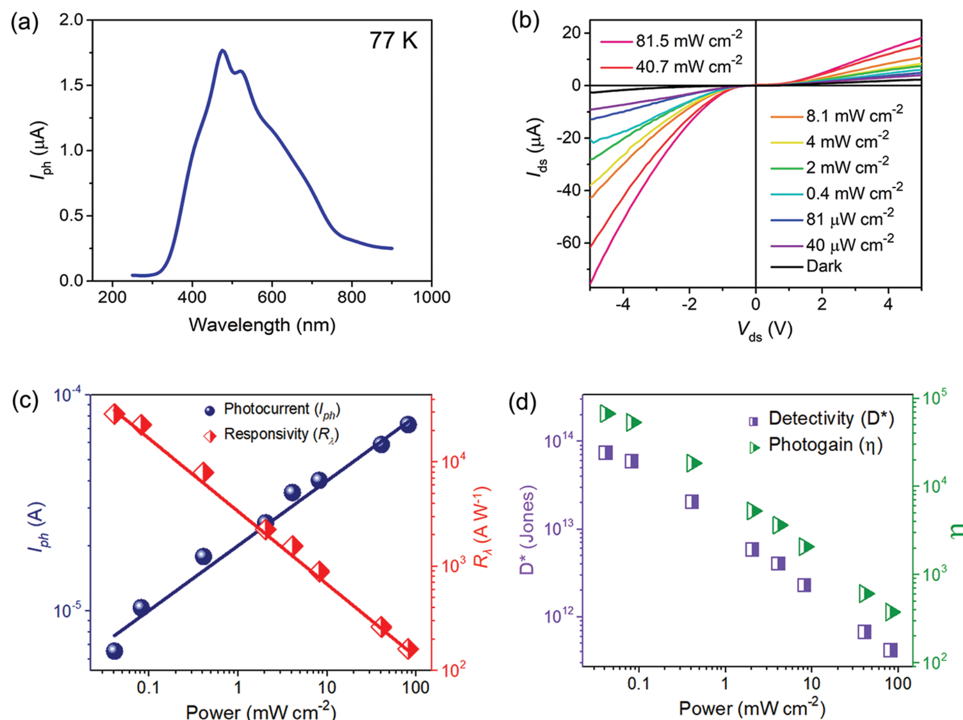

Figure 6. The photodetection performance of an anti-ambipolar *p*-SnS/*n*-$MoSe_2$ phototransistor at 77 K. a) The I_{ph} of the *p*-SnS/*n*-$MoSe_2$ device (operated at V_{sd} = 5 V and V_g = 40 V) was recorded in response to the 250–900 nm illumination generated by a Xe lamp coupled with a monochromator. b) The output curves (i.e., the $I_{sd}-V_{sd}$ plot at V_g = 40 V) of the *p*-SnS/*n*-$MoSe_2$ phototransistor were measured with 532-nm illumination of various power densities. c) (left ordinate) The I_{ph} was measured as a function of incident 532-nm laser density with the device operated at V_{sd} = 10 V and V_g = 0 V. (right ordinate) The R_λ in response to various 532-nm laser densities was measured at V_{sd} = −5 V and V_g = 40 V. d) The D^* and η were determined as a function of 532-nm laser density with the device operated at V_{sd} = −5 V and V_g = 40 V.

phototransistor gives rise to a remarkable broad spectral photoresponse at 250–900 nm with high $R_\lambda \approx 2 \times 10^4$ A W^{-1} and $D^* \approx 7.5 \times 10^{13}$ Jones measured by 532-nm laser excitation of s40 μW cm^{-2}. The outstanding performance of the *p*-SnS/*n*-$MoSe_2$ phototransistor operated at 77 K marks its potential for optoelectronics operating at cryogenic conditions in applications such as space exploration. The discovered cryo-characteristics of this heterostructure can be further extended to design the binary, ternary, and quaternary inverters, which will mark a step toward realizing the MVL circuits operated in cryogenic conditions. With MVL circuits, more information can be transferred with fewer interconnects, thus ultimately reducing the size and complexity of integrated circuits.

4. Experimental Section

Device Fabrication: A dry transfer technique was used to fabricate *p*-SnS/*n*-$MoSe_2$ heterotransistors. Few-layered *n*-$MoSe_2$ nanoflakes, exfoliated mechanically from CVT-grown *n*-$MoSe_2$ bulk crystal, were transferred onto a SiO_2/Si substrate with the assistance of a PDMS stamp. Then, the CVD-grown few-layered *p*-SnS nanoflakes on a SiO_2/Si substrate, fetched specifically by a PDMS stamp, were placed precisely on top of the pre-deposited *n*-$MoSe_2$ nanoflakes on a SiO_2/Si substrate to form a heterojunction structure using a custom-made optical micromanipulator. The transfer and deposition processes of individual *n*-$MoSe_2$ and *p*-SnS nanoflakes to form *p*-SnS/*n*-$MoSe_2$ heterojunctions were facilitated with an optical microscope (Olympus, BX 51 м) equipped with a charge-coupled device (Leica, DFC495). The contact electrodes of Cr/Au (7 nm/70 nm in thickness) were deposited in a thermal evaporator with thin-bar Cu grids as a shadow mask. For comparing the optical and electrical properties of *p*-SnS/*n*-$MoSe_2$ heterotransistors, *n*-$MoSe_2$-based and *p*-SnS-based field-effect transistors were also fabricated. All fabricated devices were pre-annealed[43] and stored in vacuum conditions for further investigations.

Characterizations: Crystalline analyses of *p*-SnS and *n*-$MoSe_2$ nanoflakes by high-resolution transmission electron microscopy (HR-TEM) were conducted in a transmission electron microscope (TEM) (JEOL, JEM-2100F) with an operating voltage of 200 kV. Surface topographic scans for *p*-SnS and *n*-$MoSe_2$ nanoflakes were performed in an atomic force microscope (AFM) (Bruker Dimension Icon) to measure the height profiles of the *p*-SnS/*n*-$MoSe_2$ heterojunctions. Temperature-dependent Raman and PL spectra were acquired in a micro-Raman spectrometer (Horiba, LabRAM HR Evolution), equipped with a grating of 1800 grooves/mm, a detector (Jobin Won Horiba, SDrive-500 Syncernity), a 532 nm laser system including an optical microscope (Olympus, CX41), and a cryostat (Linkam-LTS 420). Frequency calibration of the observed Raman scattering signals was assisted by the peak of Si wafer at 520 cm^{-1}. Topological elemental mapping of the *p*-SnS/*n*-$MoSe_2$ heterostructure was conducted in a scanning electron microscope (SEM) (Jeol, JSM-7800F) equipped with an energy-dispersive spectroscopy (EDS) detector. X-ray photoelectron spectroscopy (XPS) was performed using an ESCA spectrometer (VG Scientific, Escalab 250), containing a monochromatic X-ray source (1486.6 eV Al Kα) and CASA XPS software (v.2.3.17, Casa Software Ltd., Wilmslow, UK) for spectral analysis. The binding energies of the observed signals were calibrated against the carbon C 1s peak at 284.8 eV prior to analysis. The Shirley-Sherwood method was employed to subtract the background. The work functions of *n*-$MoSe_2$ and *p*-SnS were determined by ultraviolet photoelectron spectroscopy (UPS) (ULVAC-PHI,

© 2023 The Authors. Advanced Electronic Materials published by Wiley-VCH GmbH

PHI 500 Versaprobe-II) with the He I excitation of 21.22 eV and an external potential of 10 V applied to samples. The cryo-electrical measurements were carried out using a cryo-probe station (Lakeshore, TTPX) at 10^{-3} Torr, comprising a liquid-nitrogen dewar, a cryogenic temperature controller (Lakeshore 336), and a source meter (Keithely, 2636A). The broadband photoresponse of the *p*-SnS/*n*-$MoSe_2$ heterotransistor was measured using an optical system, including a Xenon lamp (Newport, 66 921) and a monochromator (Acton, Spectrapro 500i), and a detection system containing a cryo-probe station (Lakeshore, TTPX). The wavelength-specific photoresponse and photoswitching measurements were carried out in the cryo-probe station (Lakeshore, TTPX) with an optical system of a 532 nm diode laser, a power meter (Ophir, NovaII), and an optical beam shutter (Thorlabs, SH1) controlled by LABVIEW program.

Supporting Information

Supporting Information is available from the Wiley Online Library or from the author.

Acknowledgements

R.J.M. is thankful for the support of Ms. Chia-Ying Chien of Instrumentation Center, the National Taiwan University, for her assistance in HR-TEM measurements. Special thanks to the Ministry of Science and Technology, Taiwan sponsored instrumentation centers for the characterization facilities. X.P.A.G. acknowledges the support from NSF (DMR-1607631). Y.T.C. and R.S. acknowledge the financial supports provided by the National Science and Technology Council of Taiwan under the grant numbers of 109-2113-M-A49-001-MY2, 109-2811-M-002-576, 110-2112-M-001-065-MY3, 111-2113-M-A49-037-MY2, 111-2124-M-001-009, and 111-2124-M-A49-009.

Conflict of Interest

The authors declare no conflict of interest.

Data Availability Statement

Research data are not shared.

Keywords

2D materials, anti-ambipolar transistors, low-temperature electrical transport, $MoSe_2$, photodetectors, SnS, van der Waal heterostructures

Received: February 11, 2023
Revised: April 23, 2023
Published online: May 28, 2023

[1] X. Duan, C. Wang, A. Pan, R. Yu, X. Duan, *Chem. Soc. Rev.* **2015**, *44*, 8859.
[2] Q. H. Wang, K. Kalantar-Zadeh, A. Kis, J. N. Coleman, M. S. Strano, *Nat. Nanotechnol.* **2012**, *7*, 699.
[3] M. Chhowalla, H. S. Shin, G. Eda, L. J. Li, K. P. Loh, H. Zhang, *Nat. Chem.* **2013**, *5*, 263.
[4] S. Sucharitakul, N. J. Goble, U. R. Kumar, R. Sankar, Z. A. Bogorad, F. C. Chou, Y. T. Chen, X. P. A. Gao, *Nano Lett.* **2015**, *15*, 3815.
[5] S. R. Tamalampudi, Y. Y. Lu, R. U. Kumar, R. Sankar, C. Da Liao, K. B. Moorthy, C. H. Cheng, F. C. Chou, Y.-T. Chen, *Nano Lett.* **2014**, *14*, 2800.
[6] S. Zhao, B. Dong, H. Wang, H. Wang, Y. Zhang, Z. V. Han, H. Zhang, *Nanoscale Adv.* **2020**, *2*, 109.
[7] J. A. Andrade-Arvizu, M. Courel-Piedrahita, O. Vigil-Galán, *J. Mater. Sci.: Mater. Electron.* **2015**, *26*, 4541.
[8] R. Guo, X. Wang, Y. Kuang, B. Huang, *Phys. Rev. B: Condens. Matter Mater. Phys.* **2015**, *92*, 115202.
[9] S. Sucharitakul, U. Rajesh Kumar, R. Sankar, F. C. Chou, Y. T. Chen, C. Wang, C. He, R. He, X. P. A. Gao, *Nanoscale* **2016**, *8*, 19050.
[10] Y. Wakayama, R. Hayakawa, *Adv. Funct. Mater.* **2019**, *30*, 1903724.
[11] R. J. Mathew, K. H. Cheng, C. H. Hsu, P. K. Chand, C. R. Paul Inbaraj, Y. Lou Peng, J. Y. Yang, C. H. Lee, Y. T. Chen, *Adv. Opt. Mater.* **2022**, *10*, 2102580.
[12] C. R. Paul Inbaraj, R. J. Mathew, R. K. Ulaganathan, R. Sankar, M. Kataria, H. Y. Lin, Y.-T. Chen, M. Hofmann, C.-H. Lee, Y.-F. Chen, *ACS Nano* **2021**, *15*, 8686.
[13] E. Wu, Y. Xie, Q. Liu, X. Hu, J. Liu, D. Zhang, C. Zhou, *ACS Nano* **2019**, *13*, 5430.
[14] Y. Li, Y. Wang, L. Huang, X. Wang, X. Li, H. X. Deng, Z. Wei, J. Li, *ACS Appl. Mater. Interfaces* **2016**, *8*, 15574.
[15] J. Dong, F. Liu, F. Wang, J. Wang, M. Li, Y. Wen, L. Wang, G. Wang, J. He, C. Jiang, *Nanoscale* **2017**, *9*, 7519.
[16] C. J. Park, H. J. Park, J. Y. Lee, J. Kim, C. H. Lee, J. Joo, *ACS Appl. Mater. Interfaces* **2018**, *10*, 29848.
[17] A. Nourbakhsh, A. Zubair, M. S. Dresselhaus, T. Palacios, *Nano Lett.* **2016**, *16*, 1359.
[18] E. Gutiérrez-D, J. Deen, C. Claeys, in *Low Temperature Electronics:Physics, Devices, Circuits, and Applications*, 1st ed., Elsevier, Amsterdam **2000**.
[19] M. Tan, C. Hu, Y. Lan, J. Khan, H. Deng, X. Yang, P. Wang, X. Yu, J. Lai, H. Song, *Small* **2017**, *13*, 1702024.
[20] W. Hu, H. Cong, W. Huang, Y. Huang, L. Chen, A. Pan, C. Xue, *Light: Sci. Appl.* **2019**, *8*, 106.
[21] F. P. García De Arquer, A. Armin, P. Meredith, E. H. Sargent, *Nat. Rev. Mater.* **2017**, *2*, 16100.
[22] S. Sherrit, *Smart Struct. Mater. 2005: Active Mater: Behav. Mech.* **2005**, *5761*, 335.
[23] W. Uddin, V. Dhyani, G. Ahmad, V. Kumar, P. K. Muduli, S. Das, *ACS Appl. Electron. Mater.* **2020**, *2*, 1567.
[24] D. Nam, J. U. Lee, H. Cheong, *Sci. Rep.* **2015**, *5*, 17113.
[25] A. S. Sarkar, S. K. Pal, *ACS Omega* **2017**, *2*, 4333.
[26] M. Li, Y. Wu, T. Li, Y. Chen, H. Ding, Y. Lin, N. Pan, X. Wang, *RSC Adv.* **2017**, *7*, 48759.
[27] H. R. Chandrasekhar, R. G. Humphreys, U. Zwick, M. Cardona, *Phys. Rev. B* **1977**, *15*, 2177.
[28] M. Öper, Y. Shehu, N. K. Perkgöz, *Semicond. Sci. Technol.* **2020**, *35*, 115020.
[29] S. Lin, A. Carvalho, S. Yan, R. Li, S. Kim, A. Rodin, L. Carvalho, E. M. Chan, X. Wang, A. H. Castro Neto, J. Yao, *Nat. Commun.* **2018**, *9*, 1455.
[30] G. W. Shim, K. Yoo, S. B. Seo, J. Shin, D. Y. Jung, I. S. Kang, C. W. Ahn, B. J. Cho, S. Y. Choi, *ACS Nano* **2014**, *8*, 6655.
[31] S. Tongay, J. Zhou, C. Ataca, K. Lo, T. S. Matthews, J. Li, C. Grossman, J. Wu, *Nano Lett.* **2012**, *12*, 5576.
[32] C. H. Lee, G. H. Lee, A. M. Van Der Zande, W. Chen, Y. Li, M. Han, X. Cui, G. Arefe, C. Nuckolls, T. F. Heinz, J. Guo, J. Hone, P. Kim, *Nat. Nanotechnol.* **2014**, *9*, 676.
[33] K. Kobashi, R. Hayakawa, T. Chikyow, Y. Wakayama, *ACS Appl. Mater. Interfaces* **2018**, *10*, 2762.
[34] N. Ansari, F. Ghorbani, *J. Opt. Soc. Am. B* **2018**, *35*, 1179.
[35] H. Choi, N. Lee, H. Park, Y. Choi, K. Kim, Y. Choi, J. Kim, S. Song, H. Yuk, H. Jeon, *Appl. Sci.* **2019**, *9*, 4606.

© 2023 The Authors. Advanced Electronic Materials published by Wiley-VCH GmbH

2199160x, 2023, 8, Downloaded from https://onlinelibrary.wiley.com/doi/10.1002/aelm.202300095 by National Yang Ming Chiao Tung Unive, Wiley Online Library on [14/08/2023]. See the Terms and Conditions (https://onlinelibrary.wiley.com/terms-and-conditions) on Wiley Online Library for rules of use; OA articles are governed by the applicable Creative Commons License

[36] S. Ghatak, A. N. Pal, A. Ghosh, *ACS Nano* **2011**, *5*, 7707.
[37] W. Wang, W. Wang, Y. Meng, Q. Quan, Z. Lai, D. Li, P. Xie, S. P. Yip, X. Kang, X. Bu, D. Chen, C. Liu, J. C. Ho, *ACS Nano* **2022**, *16*, 11036.
[38] R. K. Ulaganathan, Y. Y. Lu, C. J. Kuo, S. R. Tamalampudi, R. Sankar, K. M. Boopathi, A. Anand, K. Yadav, R. J. Mathew, C. R. Liu, F. C. Chou, Y. T. Chen, *Nanoscale* **2016**, *8*, 2284.
[39] C. R. Paul Inbaraj, V. K. Gudelli, R. J. Mathew, R. K. Ulaganathan, R. Sankar, H. Y. Lin, H. I. Lin, Y. M. Liao, H. Y. Cheng, K. H. Lin, F. C. Chou, Y. T. Chen, C. H. Lee, G. Y. Guo, Y. F. Chen, *ACS Appl. Mater. Interfaces* **2019**, *11*, 24269.
[40] C. R. Paul Inbaraj, R. J. Mathew, G. Haider, T. P. Chen, R. K. Ulaganathan, R. Sankar, K. P. Bera, Y. M. Liao, M. Kataria, H. I. Lin, F. C. Chou, Y. T. Chen, C. H. Lee, Y. F. Chen, *Nanoscale* **2018**, *10*, 18642.
[41] C. Xie, C. Mak, X. Tao, F. Yan, *Adv. Funct. Mater.* **2016**, *27*, 1603886.
[42] X. Gong, M. Tong, Y. Xia, W. Cai, J. S. Moon, Y. Cao, G. Yu, C. L. Shieh, B. Nilsson, A. J. Heeger, *Science* **2009**, *325*, 1665.
[43] R. J. Mathew, C. R. P. Inbaraj, S. Raman, S. M. Hudie, R. D. Nikam, C.-A. Tseng, C.-H. Lee, Y.-T. Chen, *J. Mater. Chem. C* **2019**, *7*, 10996.

© 2023 The Authors. Advanced Electronic Materials published by Wiley-VCH GmbH

2199160x, 2023, 8, Downloaded from https://onlinelibrary.wiley.com/doi/10.1002/aelm.202300095 by National Yang Ming Chiao Tung Unive, Wiley Online Library on [14/08/2023]. See the Terms and Conditions (https://onlinelibrary.wiley.com/terms-and-conditions) on Wiley Online Library for rules of use; OA articles are governed by the applicable Creative Commons License